Compressive response of lattice structures: a multiscale approach to model the influence of internal defects

Progress in Additive Manufacturing (2025) 10:4107–4121
https://doi.org/10.1007/s40964-025-01026-3

RESEARCH

Compressive response of lattice structures: a multiscale approach to model the influence of internal defects

Alberto Ciampaglia[1,2] · Carlo Boursier Niutta[1,2] · Alessandro Benelli[3,2] · Andrea Tridello[1,2]

Received: 24 December 2024 / Accepted: 13 February 2025 / Published online: 16 March 2025

Abstract
This paper presents a multiscale strategy for modeling the degrading influence of internal defects on the compressive mechanical response of an octet truss lattice structure produced by Powder Bed Fusion and made of AlSi10Mg alloy. Starting from micro-CT scans of a $2\times2\times2$ lattice structure, the internal defects population is determined and Finite Element Analyses (FEAs) are performed on Representative Volume Elements, i.e., the strut with internal defect, to determine the effective stress–strain response for each defect size. The stress–strain curves are used as material response randomly assigned to each element of the FE model of the lattice structure. By randomly varying the location of the defects within the specimen, the scatter of the compressive response can be accounted for. The effectiveness of the proposed approach is shown by comparison with the experimental results of compressive tests on $2\times2\times2$ and $3\times3\times3$ lattice specimens.

Keywords Multiscale · Compression · Damage-tolerant · Experimental · Numerical

1 Introduction

Additive manufacturing (AM) has become a key production technology, recognized as a pillar of the Industry 4.0 revolution [1, 2]. AM enables the creation of components with optimized shapes and material distribution tailored for specific applications [3–5]. Unconstrained design has promoted the development of innovative structural solutions that efficiently distributes the material to accomplish any combination of strength, stiffness, and lightweight requirements [6–11]. The advent of AM promoted the development of lattice structures [12–15], which are challenging to produce using traditional manufacturing.

Lattice structures are designed to either enhance the mechanical properties, like stiffness and strength [16–20] or unlock exotic material response (e.g., Poisson's ratio [21–23], shape memory [24, 25]). They can also replace honeycomb core [12] or serve as fillers for lightweight design [26, 27], with the unit cell optimized for the specific application. Researchers have focused on optimizing these structures to achieve exceptional homogenized properties while minimizing cell density [12, 28, 29].

Despite these advantages, structural integrity concerns persist, particularly for in-service applications [30–32]. Current design methodologies must be validated or revised to address AM-specific microstructures [33, 34] and defects [35, 36]. New design approaches are needed particularly for innovative structural solutions that are specifically developed for AM production, such as lattice structures [37, 38].

The primary challenge lies in deviations between ideal and manufactured geometries caused by defects formed during the AM process [39–42]. These defects can initiate damage, promote fatigue cracks, or reduce local stiffness and strength [43–45]. For example, the variability in material properties due to randomly distributed defects significantly impacts compressive properties, often triggering premature collapse [46, 47].

✉ Alberto Ciampaglia
alberto.ciampaglia@polito.it

Carlo Boursier Niutta
carlo.boursier@polito.it

Alessandro Benelli
alessandro.benelli@polito.it

Andrea Tridello
andrea.tridello@polito.it

[1] Department of Mechanical and Aerospace Engineering, Politecnico di Torino, Turin, Italy

[2] Inter-Departmental Multi-Disciplinary Research Centre J-TECH @PoliTO, Turin, Italy

[3] Department of Applied Science and Technology, Politecnico di Torino, Turin, Italy

Accurate models accounting for these defects are essential for predicting mechanical behavior.

Finite Element Analyses (FEAs) are widely used to study stress distribution in lattice structures [41, 48, 49]. However, simulating such small-scale geometries is computationally intensive, necessitating simplified models [43, 50–52]. For instance, in [53], an equivalent diameter was introduced to account for discrepancies between the ideal and the manufactured strut geometries in octet-truss Ti6Al4V specimens modeled with 1D elements. Micro-CT inspections revealed thinner struts than designed, with equivalent diameters improving simulation accuracy.

Similarly, [9] showed that geometric imperfections, such as strut waviness and thickness variation, significantly affect stiffness and failure modes. Other studies modeled defects as circular voids or sinusoidal surface roughness in thin struts, demonstrating reduced mechanical performance [54]. In [43], a double-diameter correction modeled defect influence in PA-12 lattice structures, enabling simplified yet accurate simulations.

Homogenization techniques, increasingly combined with machine learning, have also been explored to reduce computational demands [55]. For example, [56] studied the influence of geometric imperfections on the elastic properties of 2D and 3D periodic trusses by introducing randomly spaced defects in Representative Volume Elements (RVEs). In [51], a micro-CT-based approach simulated compressive responses of AlSi10Mg octet-truss lattice structures using 1D beam elements to balance accuracy and computational efficiency.

The analysis of existing literature highlights significant advancements in simulating the mechanical behavior of AM lattice structures, particularly through defect characterization and modeling techniques. However, many studies rely on simplified approaches, such as equivalent diameters [9, 51, 53] or defect-based corrections [39, 43], while computationally efficient, lack the integration of detailed defect data into multiscale frameworks. Other approaches, like homogenization techniques and machine learning [55, 56], have reduced computational effort but often overlook the critical influence of defects on mechanical performance. Additionally, experimental validation is frequently limited or absent, restricting the applicability of these methods for real-world applications.

In this study, we propose a multiscale methodology for simulating the compressive response of AM lattice structures, specifically Powder Bed Fusion (PBF) AlSi10Mg specimens with octet-truss unit cells. The novelty of our approach lies in integrating defect populations—assessed via high-resolution micro-CT inspections—into Representative Volume Element (RVE) simulations to accurately model defect influence on stress–strain behavior. These RVE-derived results are transferred to lattice-scale simulations using 1D beam elements, enabling efficient modeling of large-scale structures. Surface roughness is accounted for through an effective diameter derived from micro-CT data, while random defect distributions are incorporated to produce scatter bands in the force–displacement response, capturing the inherent variability of AM processes.

The methodology is validated against experimental compression tests on $2\times2\times2$ and $3\times3\times3$ lattice specimens, demonstrating its strengths and limitations compared to prior works [51, 57].

2 Materials and experiments

2.1 Additive manufacturing of AlSi10Mg specimens

2.1.1 AlSi10Mg: AM process and lattice structure specimens

The experimental activity has been carried out on AlSi10Mg specimens produced by PBF (Beam-It, Italy). The process parameters were optimized by the supplier for industrial applications, using a 30 µm layer thickness. After production, specimens underwent the Beam It Aging heat treatment at 200°C to relieve residual stress. The chemical composition of the AlSi10Mg powder, with an average size of 45 µm (D10 = 33 µm, D90 = 62 µm), is detailed in Table 1.

The experimental activity characterized the compressive response of AlSi10Mg specimens using an octet-truss unit cell (Fig. 1a) optimized in a previous study [58]. The geometry, created in Creo (PTC Inc., USA), features a nominal strut diameter of 1.5 mm and a cell size of 9 mm. Two specimen sizes were tested:

- $2\times2\times2$: Cubic specimens with 2 cells per side (1 test, Fig. 1b).
- $3\times3\times3$: Cubic specimens with 3 cells per side (2 tests, Fig. 1c).

Standard dog-bone specimens, produced using the same process parameters as the lattice structures, were subjected to quasi-static tests to determine the material properties for the Finite Element Model. Details of the experimental tests are provided in Sect. 2.3.

Table 1 Chemical composition of the AlSi10Mg powder used for the experimental activity

Si	Mg	Cu	Ni	Fe	Mn	Ti	Al
10	0.4	< 0.03	< 0.05	< 0.5	< 0.4	< 0.15	bal

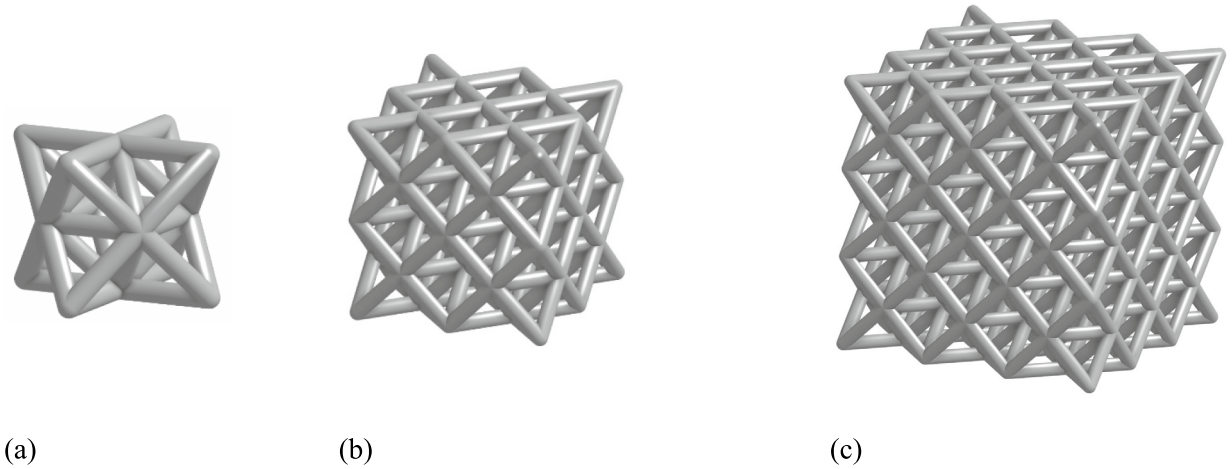

Fig. 1 AlSi10Mg lattice structure specimens subjected to experimental tests (not in scale): **a** octet truss unit cell; **b** 2×2x2 specimen; **c** 3×3x3 specimen

2.2 Lattice structure defects: computed tomography and scanning electron microscope analyses

Internal defect analysis was performed using a custom X-ray computed tomography (CT) system at J-Tech@PoliTO, equipped with a 300 kV X-ray source, 5 µm focal spot size, and a 2048×2048 pixel flat panel detector.

The optimized scanning parameters for defects analysis included:

- Scanning Parameters: 140 kV voltage, 80 µA current (11.2 W power), 1200 mm source-to-detector distance, and 150 mm source-to-sample distance, achieving a spatial resolution of 25 µm/voxel.
- Filtering: A 0.2 mm Cu filter minimized noise and enhanced reconstructed volume quality.

The 3D volumes were reconstructed using the filtered back-projection algorithm in VG MAX 3.5 (Volume Graphics GmbH, DE) from 1600 projections. Defects were identified via greyscale threshold voxel analysis, using a software-property algorithm. To reduce artifacts, material within 30 µm of the surface was excluded, and defects smaller than 0.0004 mm^3 (below the system's resolution) were disregarded as they do not impact compressive response.

Figure 2 shows the reconstructed volume of the 2×2×2 lattice sample analyzed with micro-CT.

Figure 2a shows high defectiveness in the specimen, with defects of varying sizes randomly and uniformly distributed. The histogram in Fig. 3a illustrates the maximum defects diameter for the 2×2×2 specimen. This maximum diameter, representing the largest permissible defect size, is a key parameter affecting compressive response, particularly when it lies in the beam's cross section. Other descriptors, such as equivalent diameter or projected area, could also be considered [44]. The choice of defect descriptor is further detailed in Sect. 3.1. The total material volume of the analyzed specimens is 1.89×10^{12} μm^3, with a defect volume ratio of 0.44%.

The sphericity of a defect is a key parameter for AM parts as it captures the irregular morphology of defects in addition to their size. As defined in the VG MAX 3.5 manual, sphericity is the ratio of the surface area of a sphere with the same volume as the defect to the actual surface area of the defect. Defects with sphericity near 0 have more irregular shapes. Figure 3b shows the relationship between sphericity and maximum defect diameter in the 2×2×2 specimen.

Figure 3b shows that sphericity decreases with increasing defect diameter, with larger defects exhibiting more irregular shapes (sphericity < 0.5). This aligns with literature trends [59] and highlights the critical impact of large defects on compressive response as they can locally weaken the trusses and initiate failure. Figure 3a further illustrates the significant scatter in defect distribution, contributing to the variability in mechanical response and complicating stress assessment during design. Additionally, SEM observations were conducted to examine surface roughness, which was incorporated into the numerical model using an equivalent diameter [43, 53]. Figure 4 shows the surface finish for the 2×2×2 specimen (Fig. 4a) and the 3×3×3 specimen (Fig. 4b).

2.3 Experimental tests

2.3.1 Tensile tests for material characterization

To determine the quasi-static properties of the AlSi10Mg alloy for FE analyses of lattice structures, tensile tests

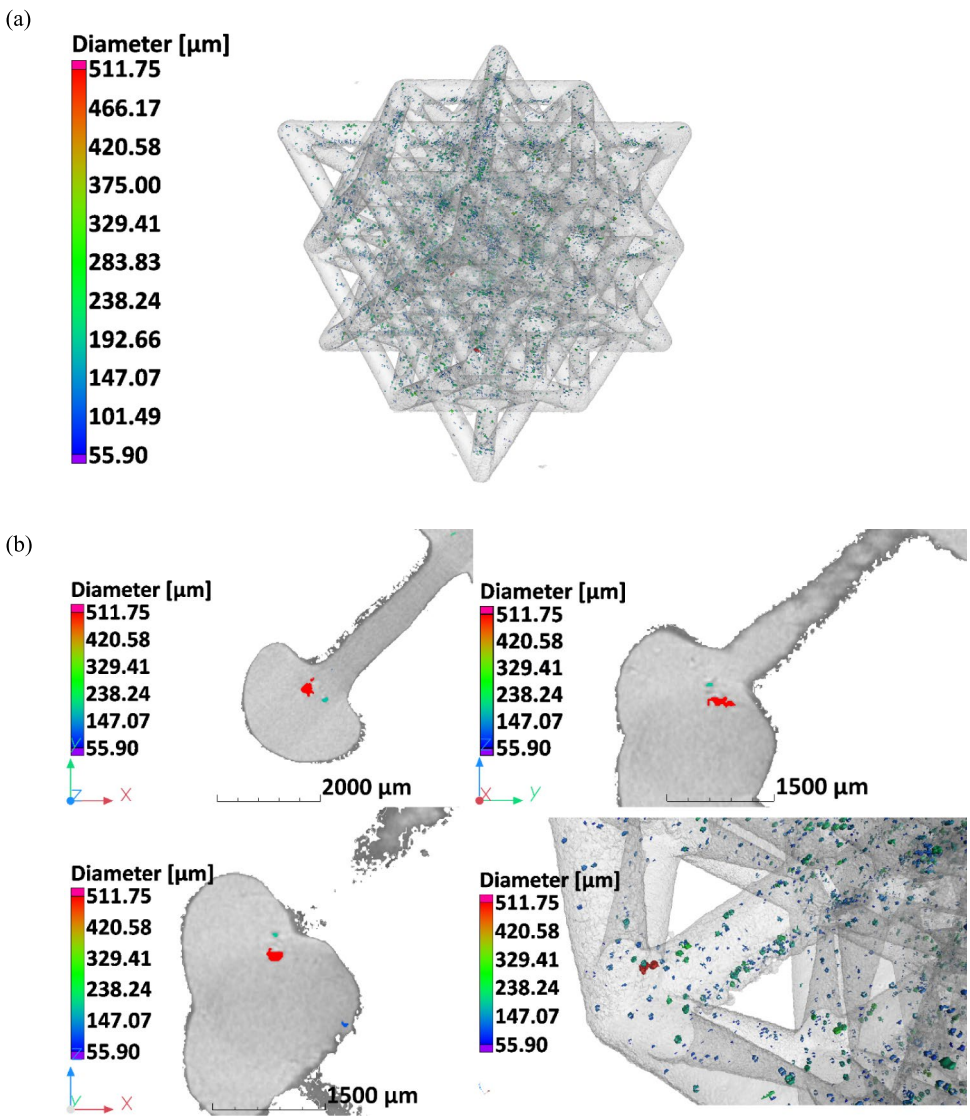

Fig. 2 Reconstructed volumes after micro-CT inspections: **a** 2×2x2 specimen; **b** largest defect in terms of diameter

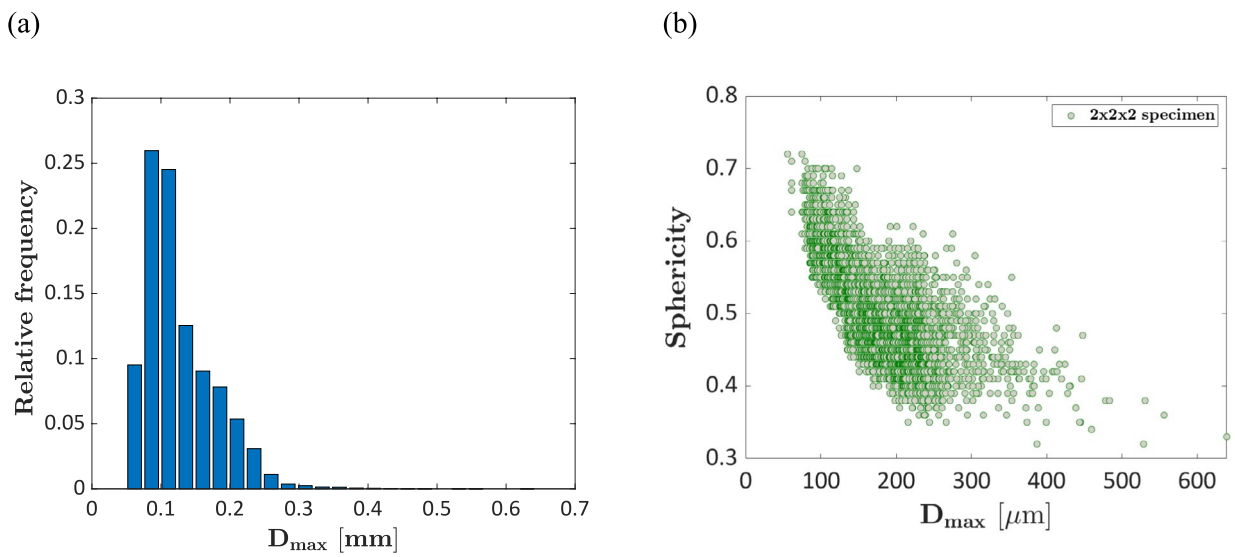

Fig. 3 **a** Histogram of the defect diameter and **b** sphericity with respect to the maximum diameter in the 2×2×2 lattice sample

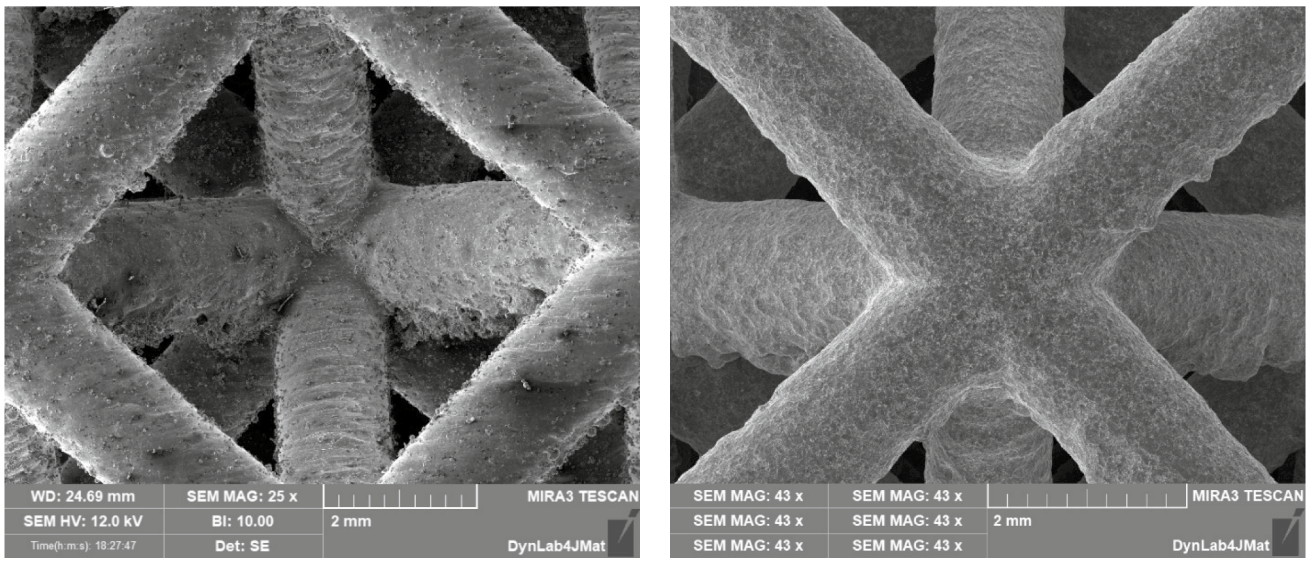

Fig. 4 Surface defect analysis using Scanning Electron Microscope (SEM); **a** 2×2×2 specimen, **b** 3×3×3 specimen

were performed on standard dog bone specimens with a 4×10 mm cross section and a 100 mm free span [57]. Two specimens were tested on an Instron 8801 servo hydraulic machine at a 1 mm/min crosshead displacement rate. Strain was measured using Digital Image Correlation (DIC) to capture the necking region and derive the true stress–true strain curve. Images were processed with VIC 3D 9.1.6 software, using a subset size of 30 px and a step size of 7 px, maintaining a step-to-subset ratio below 1/3 as recommended [60].

Figure 5 shows minimal discrepancy between the stress–strain curves of the tested specimens. The average Young's modulus was 72 GPa, yield stress 220 MPa, and strain at failure 10.5%. The averaged plastic region of the true stress–true strain curve was used in the numerical model.

However, literatures [61, 62] suggest that lattice strut properties may differ from bulk material. To verify the local elastic modulus of the struts, nano-indentation tests were conducted as detailed in the next section.

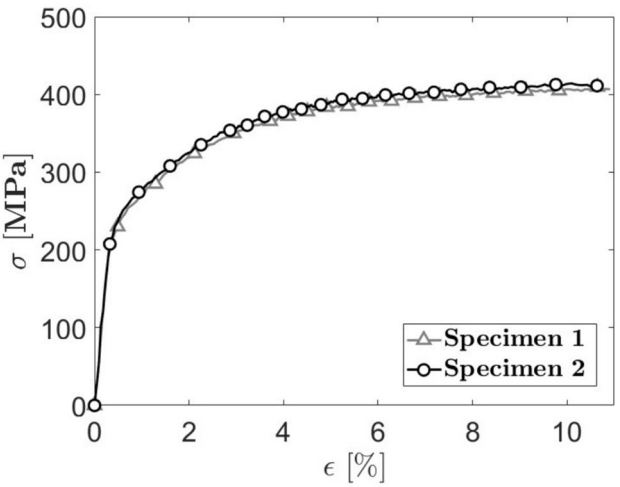

Fig. 5 True stress–true strain curves tested AlSi10Mg specimens

2.3.2 Nano-indentation test

The elastic properties of PBF-produced metal alloys vary within the part due to differing thermal histories, which impact microstructure and mechanical behavior. Consequently, tensile testing on rectangular specimens is unsuitable for characterizing lattice beam materials. Instead, nano-indentation was employed to measure the Young's modulus of AlSi10Mg directly on lattice trusses.

Nano-indentation tests were conducted using a Nanovea CB500 nano-indenter equipped with a 200N piezoresistive load cell and a diamond Berkovich tip. Two samples were prepared with material extracted from vertical (VT) and diagonal (DT) trusses. The lattice beams were embedded in epoxy, polished, and flattened for accuracy. The Young's modulus was calculated using the Oliver–Pharr method [63], where the indentation area A_p and the reduced modulus E_r of the contact bodies are related by the Hertzian theory with Eq.:

$$E_r = \frac{\sqrt{\pi}}{2}\frac{S}{\sqrt{A_p}} \quad (1)$$

where S is the slope of the unloading curve at the maximum displacement point, A_p is the projected area adjusted to account for the tip rounding though the contact depth at full load and the surrounding deformation. Indentations were performed at the center of the beam's cross-sectional surface under load control ranging from 80 to 250 mN, gradually increased until convergence of the measured module (Fig. 6). Additional tests were conducted on lattice nodes to assess stiffness variability between trusses and intersections.

Young's modules have been calculated using Eq. 1 applied to the unloading curves in Fig. 6. The results in Fig. 6c indicate convergence to E = 53 GPa, significantly lower than the value obtained from tensile tests on the bar as it has been previously observed in the literature [62]. This discrepancy could be due to the different thermal history of the fused material in the lattice beam and the bar. For subsequent analyses, the local elastic modulus of the pristine AlSi10Mg truss is taken as E = 53 GPa.

2.3.3 Compression tests of lattice specimens

Quasi-static compression tests were conducted on 2 × 2 × 2 and 3 × 3 × 3 lattice specimens using a Zwick Roell Z050 electrodynamic machine with a 50 kN load cell. The crosshead displacement rate was set to 1 mm/min to minimize inertial and strain rate effects. Force–displacement curves from these tests were used to validate the proposed multiscale approach. Additional details on the test configuration and 3 × 3 × 3 specimen tests are available in [57].

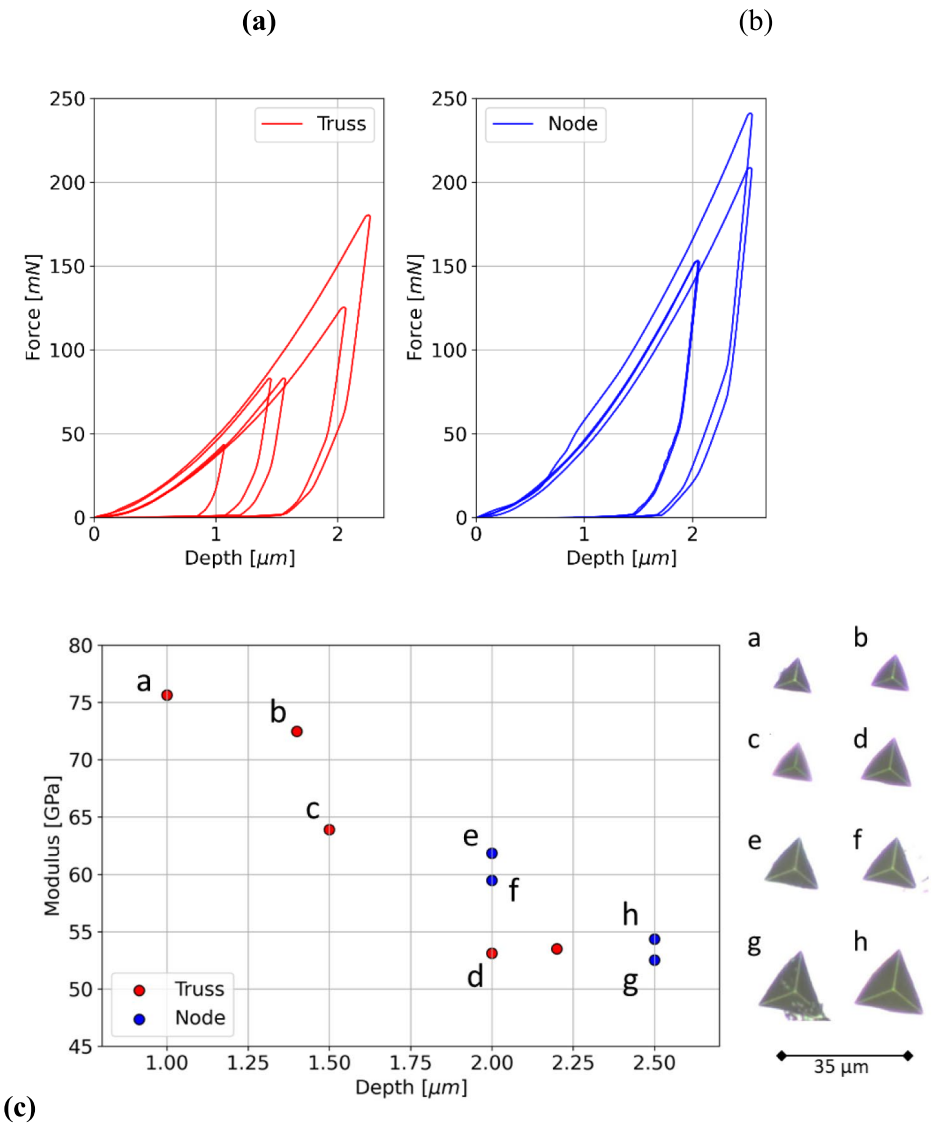

Fig. 6 The load–depth curves measured during the nanoindentation tests on the truss **a** and the node **b** and the calculated Young's modulus **c**

3 Multiscale models of the as-built lattice cell

3.1 Representative Volume Element of the as-built AlSi10Mg

This section outlines a multiscale numerical strategy to model microstructural variability in AM structures. Inhomogeneities at the lower scale are represented within an RVE to compute the homogenized material response, which is then applied at the higher scale to evaluate defect effects on structural performance.

The approach assumes an inhomogeneous RVE with known constituent behaviors, enabling computational homogenization using:

$$\begin{cases} \overline{\sigma} = \frac{1}{V(\Omega)} \int_{\Omega} \boldsymbol{\sigma}(\boldsymbol{x}) dV \\ \overline{\varepsilon} = \frac{1}{V(\Omega)} \int_{\Omega} \boldsymbol{\varepsilon}(\boldsymbol{x}) dV \end{cases} \tag{2}$$

where $\overline{\sigma}$ and $\overline{\varepsilon}$ are the homogenized stress and strain, respectively, while σ and ε are the stress and strain fields in the RVE when specific boundary conditions (BC) are applied. The BCs must comply with the Hill-Mandel macro-homogeneity principle:

$$\overline{\sigma} : \dot{\overline{\varepsilon}} = \int_{\Omega} \boldsymbol{\sigma}(\boldsymbol{x}) : \dot{\boldsymbol{\varepsilon}}(\boldsymbol{x}) dV \tag{3}$$

If Eq. 3 is satisfied, the variation of the strain energy density is also preserved in the homogenization process.

In this work, the RVE of the lattice truss containing a manufacturing defect is a cylindrical RVE (CY-RVE) with a randomly positioned defect (as shown in Fig. 7).

Common cubic RVEs assume 3D material periodicity, while CY-RVEs limit periodicity to the truss's axial dimension, modeling its response for a given diameter and arbitrary length.

Linear Kinematic Boundary conditions (LKBCs) are used:

$$u_i = \overline{\varepsilon}_{ij} x_j, \; x \in \partial_D \Omega \tag{4}$$

The RVE size is determined through a sensitivity analysis of homogenized stiffness and yield stress (Sect. 4.1). To ensure damage propagation modeling and faster convergence, periodic microstructures are used when defects intersect RVE boundaries.

Defects in the lattice structure arise from stochastic production anomalies, forming statistically distributed defects. To capture their effect on homogenized response, a Stochastic Volume Element (SVE) is introduced, defined probabilistically based on the experimental defect distribution. Following [64], the defect equivalent diameter's cumulative density function is subsampled into discrete values, and an SVE is generated for each diameter. These SVEs are then assigned to material points, preserving the defect diameter distribution.

Bulk elastic properties are derived from nano-indentation tests, while plastic behavior is calibrated using tensile tests. The plastic response is modeled with a J2 plasticity model and an isotropic hardening law.

3.2 Multi-cell model with the manufacturing-induced variation of material properties

In this section, FE element model of the compression tests of the lattice structures is presented and detailed. The model adopts 1D beam elements to limit the computational effort without significantly affecting the simulation accuracy [65]. For the determination of the beam diameter, which consistently affects the global response of the lattice specimen, a specific procedure based on 3D FE analyses has been employed as detailed in the following.

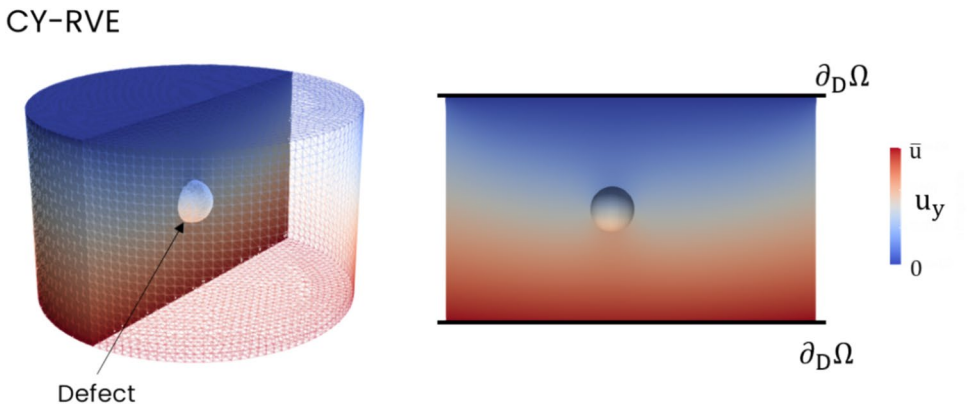

Fig. 7 **a** Geometry of a CY-RVE with an internal defect; **b** An example result of a RVE test with LKBc

3.2.1 Assessment of the effective beam diameter

Figure 4 shows significant surface roughness on the struts of the 2×2×2 lattice specimen, comparable to the strut diameter, which can impact mechanical response. SEM and micro-CT analyses reveal that surface roughness varies with orientation, being higher in horizontal struts than in inclined ones.

Previous works [53] have shown that the superficial portion of the struts contributes minimally to deformation under load. To determine an effective strut diameter, representing the deformable portion under load, the strut geometry was reconstructed from micro-CT scans and meshed with 3D tetrahedral elements using a 0.05 mm mesh size to capture surface details. Five horizontal and five inclined beams were randomly sampled from the specimen for analysis. Figure 8 illustrates the extraction locations and an example of a meshed horizontal beam.

In the LS-Dyna environment, FE linear implicit analyses were performed on the extracted beams. One surface was constrained, and a distributed force was applied to the opposite surface via rigid connections to a master node. A linear elastic isotropic material law was used. The effective diameter for the 1D beam elements of the 2×2×2 lattice model was calibrated to match the stiffness of the 3D strut model using the same strut length as the 3D model.

Table 2 lists the effective 1D beam diameters for the extracted horizontal and inclined beams, while Fig. 8 compares the real strut cross section with the corresponding effective cross section.

Table 2 shows that the average effective diameter of the 2×2×2 specimen is 1.4 mm for both horizontal and inclined struts, slightly below the nominal value of 1.5 mm.

3.2.2 FE model of the quasi-static compression of the lattice structures

Quasi-static compression tests on lattice specimens were replicated in LS-Dyna using nonlinear explicit FE analyses. The lattice was modeled with 1D beam elements using the Hughes–Liu formulation, with a 1 mm length and a diameter of 1.4 mm as determined in the previous section.

The CY-RVE simulations provided the stress–strain response for struts with varying internal defects. The defect size distribution was derived from micro-CT scans, and its probability density function was used to assign

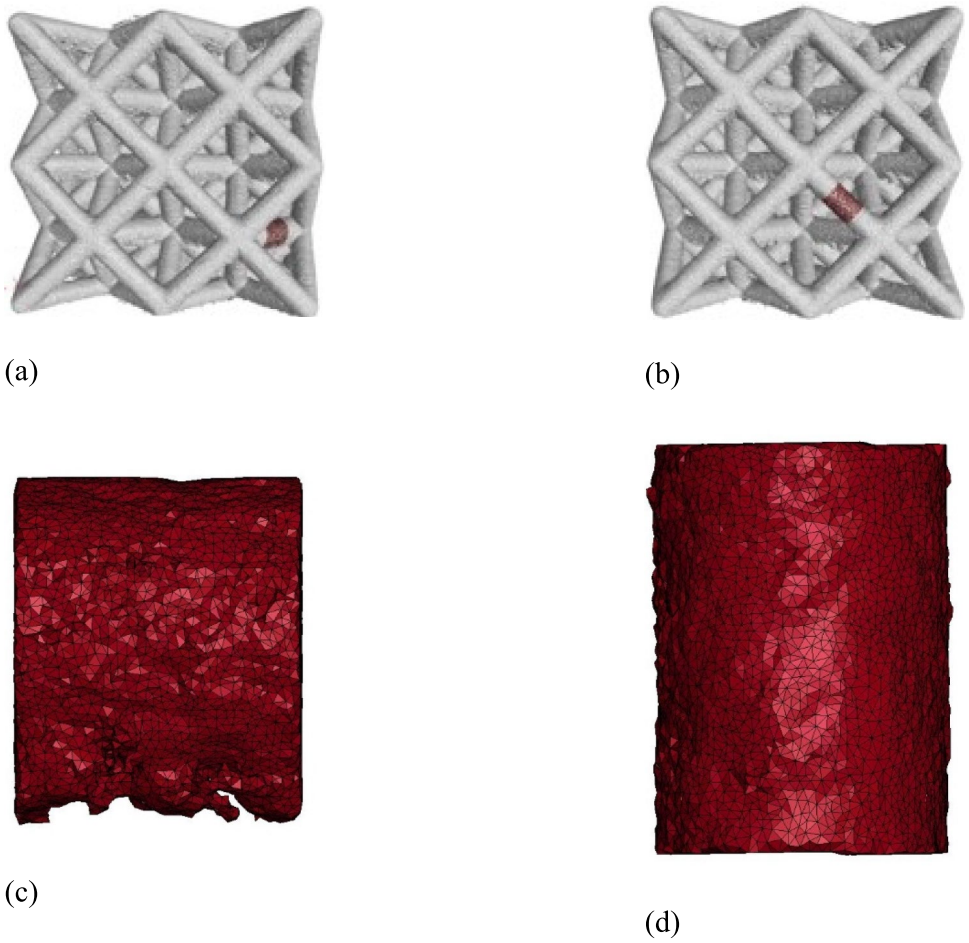

Fig. 8 Example of extractions and mesh of beams for the identification of the effective diameter: **a** horizontal strut; **b** inclined strut; **c** mesh of horizontal strut; **d** mesh of inclined strut

Table 2 Effective diameter of the equivalent 1D beam element for the horizontal and inclined struts

	Beam	Effective Diameter [mm]
Horizontal struts	1	1.42
	2	1.38
	3	1.39
	4	1.42
	5	1.40
Inclined struts	6	1.41
	7	1.42
	8	1.39
	9	1.39
	10	1.41

material properties to individual 1D elements. Specifically, a MATLAB script mapped the defect probability distribution onto the lattice, ensuring that each beam element was assigned a defect size based on random sampling from the distribution. The corresponding elasto-plastic response for each defect size was implemented in LS-Dyna using the *MAT_PIECEWISE_LINEAR_PLASTICITY material law. The total effective volume fraction of defects within the lattice was estimated based on the statistical distribution of defect sizes and their occurrence across all beam elements. It has been observed that the total defective volume computed with the micro-CT scans (8.24 mm^3), while the defective volume was equal to 3.6–4.2 mm^3, depending on the random sampling from the distribution. However, as will be shown later, smaller defects have a negligible influence on the mechanical response. If only the defects determining a reduction of the yield and ultimate strength higher than 5% are retained, the discrepancy between the experimental and the numerical porosities becomes negligible. It is worth highlighting that the whole defect volume can be accounted for by increasing the total number of 1D elements of the lattice model and accordingly the computational cost. A flowchart of the multiscale model is reported in Fig. 9.

Defect populations and locations were randomized for each simulation, and the analyses were repeated to account for variability, producing a band of responses.

The compression test setup included two rigid walls: one stationary and one compressing the structure. Walls were modeled with shell elements and a rigid material law (*MAT_RIGID) for accurate contact stiffness. Contact between walls and the lattice was defined using *CONTACT_AUTOMATIC_SURFACE_TO_SURFACE_MORTAR, while *CONTACT_AUTOMATIC_GENERAL was used for beam-to-beam self-contact, crucial during post-failure densification.

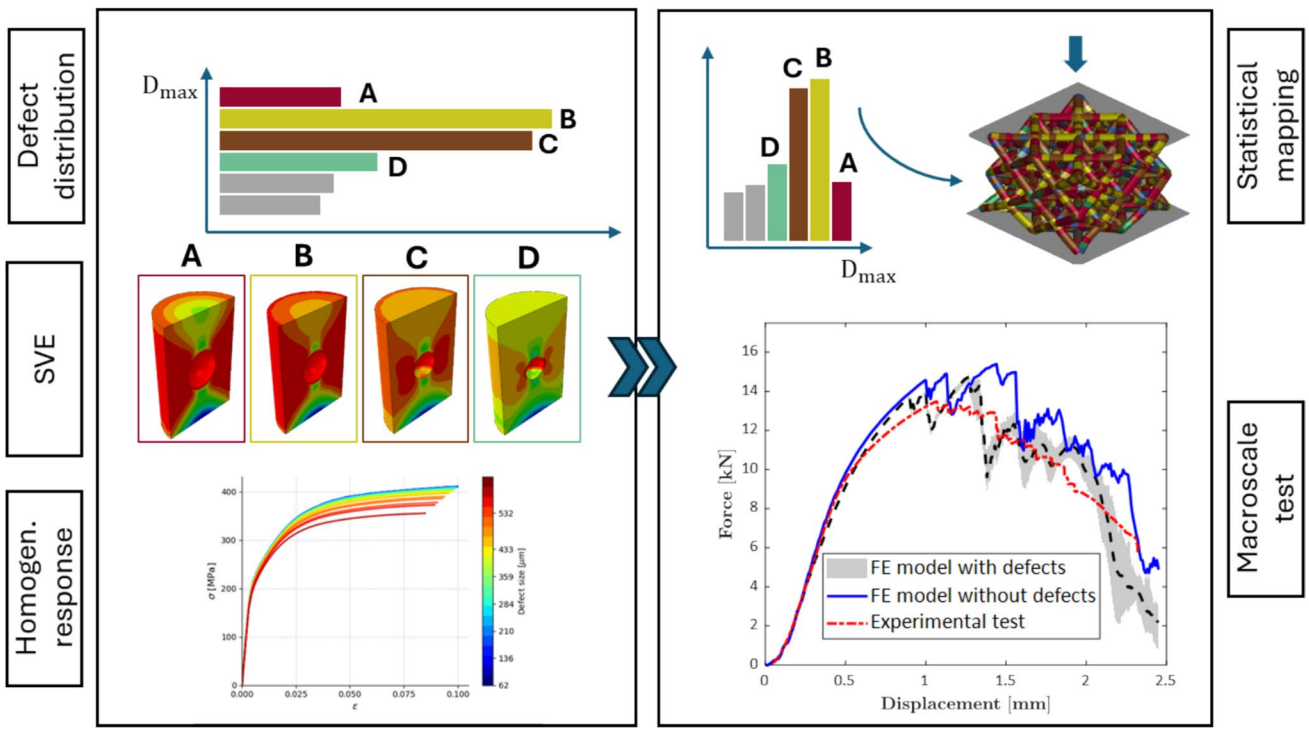

Fig. 9 Flowchart of the multiscale framework to model the effect of internal defects on the compressive response of the lattice cell

4 Results

4.1 Modeling the response of AlSi10Mg lattice beams produced by PBF

4.1.1 Micromechanics simulations of as-built lattice truss

The effect of the CY-RVE diameter was assessed by examining the convergence of the homogenized Young's modulus and yield stress across various RVE realizations with increasing sizes and different defects (Fig. 10).

The elastic modulus of the CY-RVE converges rapidly to a homogenized value at around 1 mm, while the yield stress converges more slowly. Most CY-RVEs do not achieve convergence at the nominal lattice truss diameter of 1.4 mm, as the defect scale and truss cross-sectional dimensions are not distinctly separate. Thus, only 1D axial periodicity can be modeled, making a CY-RVE with a 1.4 mm diameter appropriate.

A total of 21 CY-RVEs were generated, each representing a defect class defined by the histogram in Fig. 3. The defect diameter was set to the average of each class, while the beam diameter and the length were fixed at 1.4 mm and 2 mm. The RVE models used a global mesh size of 0.05 mm, with local refinements around defects down to 0.005 mm, resulting in approximately 500,000 elements. A 0.2 mm displacement was applied to the beam's boundary face, and simulations were performed in Abaqus CAE using a nonlinear implicit solver on 16 CPUs. The homogenized material response for each defect class (Fig. 11) was computed using the discrete form of Eq. (2), based on the stress, strain, and volume values of each mesh element.

Elastic modulus, yield stress, and maximum stress were calculated for each RVE. Yield stress was defined as the stress corresponding to 0.2% plastic deformation, while maximum stress was defined as the homogenized stress at which 10% of the RVE volume reaches the bulk material's ultimate strain at failure. Figure 12 shows how these properties vary with defect size.

The elastic modulus is minimally affected by defects, whereas maximum and yield stresses decrease as defect size increases. This reduction is attributed to stress intensification around pores, leading to local plastic zones that weaken the truss. A significant drop in maximum and yield stresses occurs when defect diameters exceed 200 µm, below which defect effects are negligible.

The material response from micromechanical simulations is transferred to the higher-scale lattice model, with each element assigned a corresponding RVE as detailed in Sect. 3.2.

4.2 Compression test of lattice cubes

This section compares the experimental and numerical results for the 2×2×2 specimen to validate the proposed multiscale approach. Additionally, it includes a comparison with experimental results for a 3×3×3 lattice specimen from [51].

4.2.1 *2×2x2 lattice specimen*

Figure 13 shows the comparison of the experimental and numerical results of the 2×2x2 lattice specimen.

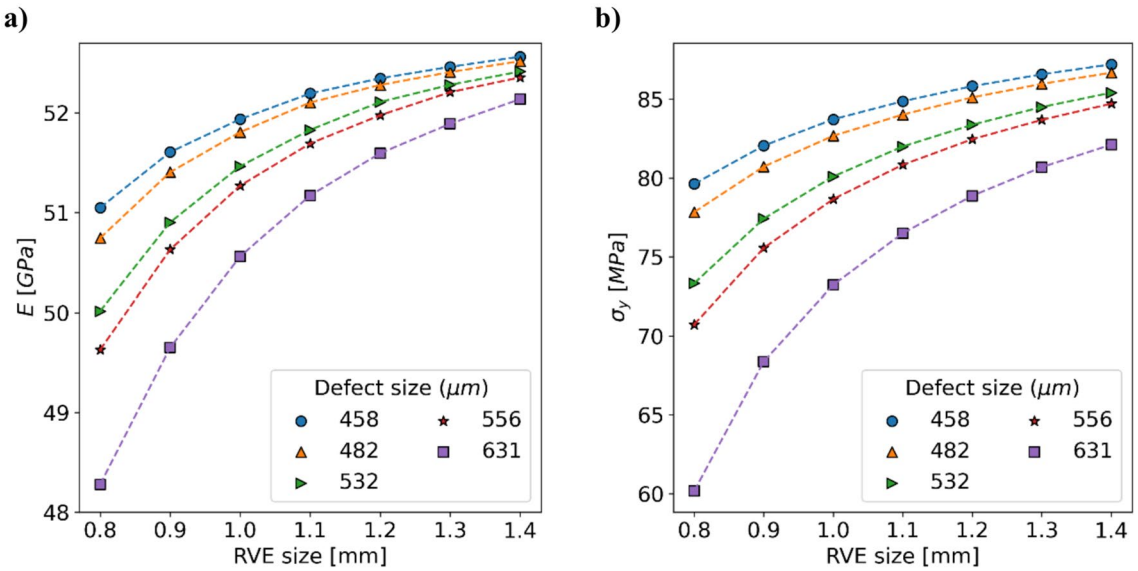

Fig. 10 Analysis of the homogeneous elastic moduli **a** and yielding stress **b** with varying diameters of the cylindrical RVE

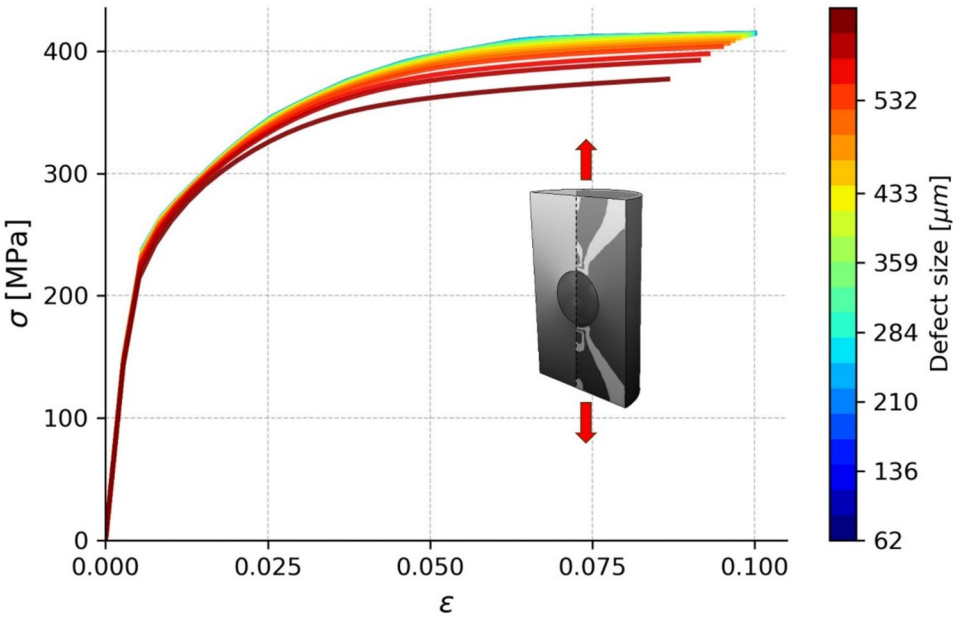

Fig. 11 Material response of the RVEs associated with the different classes of defects extracted from the micro-CT analysis

For the numerical simulations, a band of results is presented, reflecting the variability in mechanical response due to differences in defect populations and their spatial distribution within the specimen. Thirty simulations were performed, each randomly selecting defect populations and varying defect locations. The band, representing the 95% confidence interval, assumes a normal distribution of the force for each crosshead displacement. It is important to note that while the simulations respect the probability distribution of defect sizes, the rarest and largest defects were not always included due to the random selection process.

Additionally, a simulation of a defect-free specimen, with all beam elements assigned bulk material properties, is provided for comparison. Figure 13 shows that the proposed multiscale model closely matches the experimental force–displacement curve, with the numerical band oscillating around the experimental results. In contrast, the defect-free model significantly overpredicts the compressive response, particularly in terms of absorbed energy (area under the force–displacement curve). The multiscale model more accurately predicts the first peak force, with the experimental value at 13.5 kN (46.7 MPa), the defect-free model at 14.7 kN (51 MPa, 9% error), and the multiscale model ranging between 13.3–13.7 kN (46—47.5 MPa).

However, the multiscale model shows a less-pronounced plastic deformation before the first force drop compared to the experimental curve, indicating earlier failure. This brittle behavior is attributed to the failure criterion used in RVE analyses, where beams fail when at least 10% of the RVE volume reaches the ultimate strain. Developing a more refined failure criterion at the microscopic level is beyond the scope of this work. The load drops observable in the numerical results are due to the progressive failure of the beams, which lead to contact loss with the rigid wall and consequent numerical fluctuations.

In conclusion, these results demonstrate that defects impact the compressive response of lattice structures, and their influence must be properly modeled. The multiscale approach not only predicts the compression response accurately but also provides a response scatter estimate, enabling the identification of a safe lower bound for design.

4.2.2 *3 × 3x3 lattice specimen*

Figure 14 shows the comparison of the experimental and numerical results.

For the 3 × 3 × 3 specimen model, the beam diameter was set to 1.3 mm as determined in [51], while the defect population from the 2 × 2 × 2 specimen was used. As with the smaller model, 30 simulations were performed, randomizing defect populations and locations. A defect-free model was also simulated for comparison.

As shown in Fig. 14, the numerical model accurately predicts the compression response, with the scatter band aligning with experimental results. Like the 2 × 2 × 2 model, the defect-inclusive approach better predicts the first peak force compared to the defect-free model though with a slightly higher discrepancy. The experimental first peak force is in the range of 25–26.5 kN (38.4—40.8 MPa), while the defect-free model predicts 30 kN (46 MPa) and the defect-inclusive model estimates approximately 28.5 kN (43.8 MPa). This discrepancy likely arises from using the defect population of the 2 × 2 × 2 specimen as defect distributions vary between specimens and with material volume [57].

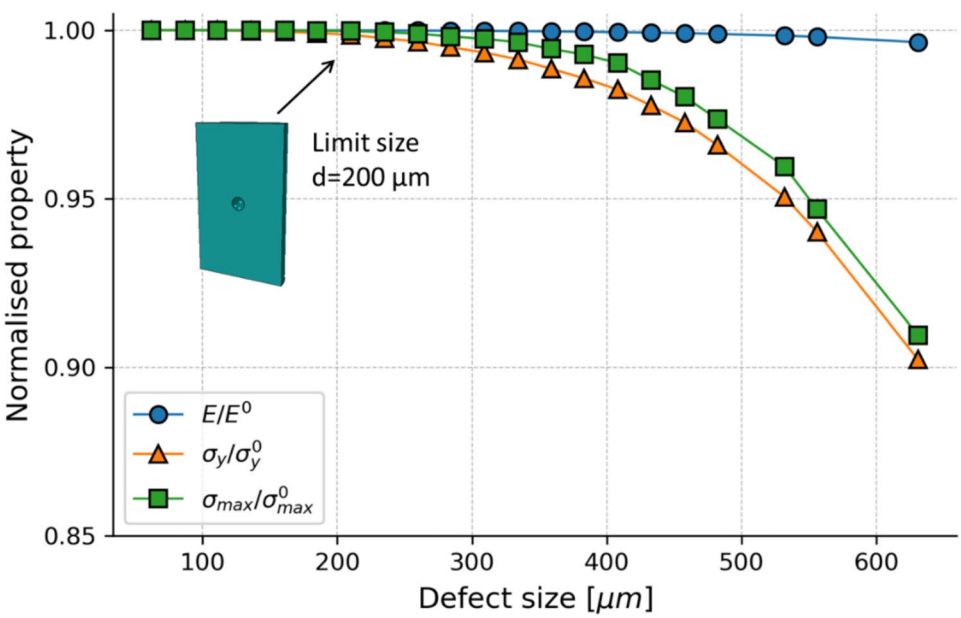

Fig. 12 Variation of the material properties with the diameter of the spherical defect

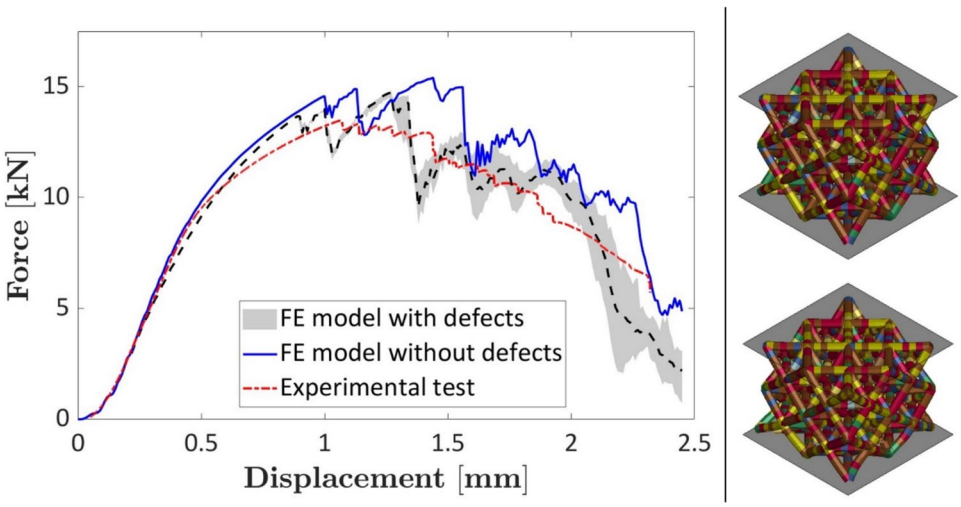

Fig. 13 Comparison of the experimental and numerical force–displacement curves of the 2×2 lattice specimen. On the right, snapshots of the lattice at its undeformed state (top) and at 1.5 mm compression (bottom), where colors indicating the different material properties related to defects

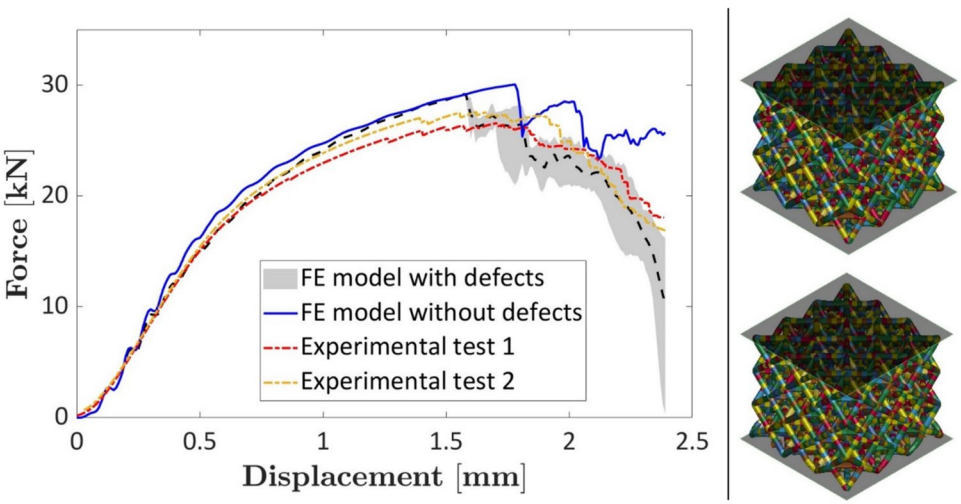

Fig. 14 Comparison of the experimental and numerical force–displacement curves of the 3×3 lattice specimen. On the right, snapshots of the lattice at its undeformed state (top) and at 2 mm compression (bottom), where colors indicating the different material properties related to defects

Despite this, the defect-inclusive model better captures the post-peak failure behavior and absorbed energy compared to the defect-free model. These findings confirm that the multiscale methodology effectively captures the degrading influence of defects on the compressive response of lattice structures. By incorporating randomized defect populations and locations, the methodology accounts for response scatter and supports the identification of a lower-bound design curve through statistical analysis.

5 Conclusions

In this work, a multiscale methodology has been proposed and validated, which accounts for the degrading influence of internal defects on the mechanical response of octet-truss lattice structure in AlSi10Mg produced by Powder Bed Fusion. Starting with defect population characterization via micro-CT scans, Finite Element Analyses (FEAs) were performed on Representative Volume Elements (RVEs) with variable defects to determine the effective stress–strain response. The resulting stress–strain curves at the microscopic level were integrated into a lattice FE model in accordance with the defect class probabilities obtained from micro-CT data. By randomizing defect populations and locations, the compressive response scatter was captured. The excellent agreement between the multiscale model and the experimental results for $2\times2\times2$ and $3\times3\times3$ specimens confirms the effectiveness of the proposed approach.

Key findings include:

- Nano-indentation tests revealed a 30% reduction in the elastic modulus of lattice struts compared to bulk material, consistent with literature [62] and attributed to the manufacturing process.
- The surface roughness, comparable to the strut diameter, affects the mechanical response. An effective diameter was determined via micro-CT reconstructions and FEAs to account for this.
- The comparison between defect-free and multiscale models highlights that internal defects significantly degrade the mechanical response, with the multiscale methodology effectively capturing this influence.
- By randomly extracting the defect population and randomly distributing the defects within the specimen, the proposed multiscale methodology can account for the response scatter of lattice structures and supporting damage-tolerant design strategies through statistical lower-bound curve identification.
- A proper microscopic failure criterion is crucial as it significantly impacts the macroscopic response, warranting careful consideration in multiscale approaches.

It should be noted that non-spherical defects with low sphericity may induce localized stress concentrations not fully captured by the micromechanical simulation with spherical voids. Future work will explore 3D modeling and refined beam discretization to assess the effects of the defect morphology.

Author contribution All authors contributed to the writing and revision of the manuscript. A.C. performed the nanoindentation tests, micro-scale simulations, and multiscale implementation, C.B. performed part-scale simulations and experimental testing, A.B. performed micro-CT analysis, and experimental testing, A.T. performed experimental testing, coordinated the project, and provided resources.

Funding Open access funding provided by Politecnico di Torino within the CRUI-CARE Agreement.

Data availability No datasets were generated or analysed during the current study.

Declarations

Conflict of Interest The authors declare no competing interests.

References

1. Mehrpouya M, Dehghanghadikolaei A, Fotovvati B, Vosooghnia A, Emamian SS, Gisario A (2019) The potential of additive manufacturing in the smart factory industrial 4.0: a review. Appl Sci. https://doi.org/10.3390/APP9183865
2. Khorasani M, Loy J, Hossein Ghasemi A, Sharabian E, Leary M, Mirafzal H, Cochrane P, Rolfe B, Gibson I (2022) A review of industry 4.0 and additive manufacturing synergy. RPJ. https://doi.org/10.1108/RPJ-08-2021-0194
3. Pollock TM, Clarke AJ, Babu SS (2020) Design and tailoring of alloys for additive manufacturing. Metall Mater Trans A Phys Metall Mater Sci 51:6000–6019. https://doi.org/10.1007/s11661-020-06009-3
4. Sobhani S, Allan S, Muhunthan P, Boigne E, Ihme M (2020) Additive manufacturing of tailored macroporous ceramic structures for high-temperature applications. Adv Eng Mater. https://doi.org/10.1002/adem.202000158
5. Mora Sierra DC, Heydari Astaraee A, Guagliano M, Bagherifard S (2022) Numerical investigation of Ti6Al4V gradient lattice structures with tailored mechanical response. Adv Eng Mater. https://doi.org/10.1002/adem.202101760

6. Zhu X, Zhang L, Tang S (2021) Adaptive selection of reference stiffness in virtual clustering analysis. Comput Methods Appl Mech Eng 376:113621. https://doi.org/10.1016/j.cma.2020.113621
7. Xie G, Dong Y, Zhou J, Sheng Z (2020) Topology optimization design of hydraulic valve blocks for additive manufacturing, Proc Inst Mech Eng C J Mech. Eng Sci 234:1899–1912. https://doi.org/10.1177/0954406220902166
8. Liu J, Ma Y (2017) Sustainable design-oriented level set topology optimization. J Mech Design. https://doi.org/10.1115/1.4035052
9. Liu L, Kamm P, García-Moreno F, Banhart J, Pasini D (2017) Elastic and failure response of imperfect three-dimensional metallic lattices: the role of geometric defects induced by Selective Laser Melting. J Mech Phys Solids 107:160–184. https://doi.org/10.1016/j.jmps.2017.07.003
10. Bendsøe MP, Sigmund O (2004) Topology optimization. Topol Optim. https://doi.org/10.1007/978-3-662-05086-6
11. Boursier Niutta C, Ciardiello R, Tridello A (2022) Experimental and Numerical investigation of a lattice structure for energy absorption: application to the design of an automotive crash absorber. Polymers. https://doi.org/10.3390/POLYM14061116
12. Pan C, Han Y, Lu J (2020) Design and optimization of lattice structures: A review. Applied Sciences (Switzerland) 10:1–36. https://doi.org/10.3390/APP10186374
13. Alkentar R, Máté F, Mankovits T (2022) Investigation of the Performance of Ti6Al4V Lattice Structures Designed for Biomedical Implants Using the Finite Element Method. Materials. https://doi.org/10.3390/MA15186335
14. Obadimu SO, Kourousis KI (2021) Compressive behaviour of additively manufactured lattice structures: a review. Aerospace. https://doi.org/10.3390/AEROSPACE8080207
15. Maconachie T, Leary M, Lozanovski B, Zhang X, Qian M, Faruque O, Brandt M (2019) SLM lattice structures: Properties, performance, applications and challenges. Mater Des 183:108137. https://doi.org/10.1016/J.MATDES.2019.108137
16. Dong G, Zhao YF (2018) Numerical and experimental investigation of the joint stiffness in lattice structures fabricated by additive manufacturing. Int J Mech Sci 148:475–485. https://doi.org/10.1016/j.ijmecsci.2018.09.014
17. Daynes S (2023) High stiffness topology optimised lattice structures with increased toughness by porosity constraints. Mater Des. https://doi.org/10.1016/j.matdes.2023.112183
18. Kechagias S, Oosterbeek RN, Munford MJ, Ghouse S, Jeffers JRT (2022) Controlling the mechanical behaviour of stochastic lattice structures: The key role of nodal connectivity. Addit Manuf. https://doi.org/10.1016/j.addma.2022.102730
19. Zhang L, Song B, Fu JJ, Wei SS, Yang L, Yan CZ, Li H, Gao L, Shi YS (2020) Topology-optimized lattice structures with simultaneously high stiffness and light weight fabricated by selective laser melting: Design, manufacturing and characterization. J Manuf Process 56:1166–1177. https://doi.org/10.1016/j.jmapro.2020.06.005
20. Li T, Jarrar F, Abu Al-Rub R, Cantwell W (2021) Additive manufactured semi-plate lattice materials with high stiffness, strength and toughness. Int J Solids Struct. https://doi.org/10.1016/j.ijsolstr.2021.111153
21. Xue X, Lin C, Wu F, Li Z, Liao J (2023) Lattice structures with negative poisson's ratio: a review. Mater Today Commun. https://doi.org/10.1016/j.mtcomm.2022.105132
22. Chen Z, Wang Z, Zhou S, Shao J, Wu X (2018) Novel negative poisson's ratio lattice structures with enhanced stiffness and energy absorption capacity. Materials. https://doi.org/10.3390/ma11071095
23. Li D, Yin J, Dong L, Lakes RS (2018) Strong re-entrant cellular structures with negative Poisson's ratio. J Mater Sci 53:3493–3499. https://doi.org/10.1007/s10853-017-1809-8
24. Roudbarian N, Jebellat E, Famouri S, Baniasadi M, Hedayati R, Baghani M (2022) Shape-memory polymer metamaterials based on triply periodic minimal surfaces. Euro J Mech A/Solids. https://doi.org/10.1016/j.euromechsol.2022.104676
25. Keshavarzan M, Kadkhodaei M, Forooghi F (2020) An investigation into compressive responses of shape memory polymeric cellular lattice structures fabricated by vat polymerization additive manufacturing. Polym Test. https://doi.org/10.1016/j.polymertesting.2020.106832
26. Guo L, Ataollah Naghavi S, Wang Z, Nath Varma S, Han Z, Yao Z, Wang L, Wang L, Liu C (2022) On the design evolution of hip implants: A review. Mater Des. https://doi.org/10.1016/j.matdes.2022.110552
27. Hou W, He P, Yang Y, Sang L (2023) Crashworthiness optimization of crash box with 3D-printed lattice structures. Int J Mech Sci. https://doi.org/10.1016/j.ijmecsci.2023.108198
28. Fernandes RR, Tamijani AY (2021) Design optimization of lattice structures with stress constraints. Mater Des. https://doi.org/10.1016/j.matdes.2021.110026
29. Park KM, Min KS, Roh YS (2021) Design optimization of lattice structures under compression: study of unit cell types and cell arrangements. Materials. https://doi.org/10.3390/MA15010097
30. Zhang X, Liang E (2019) Metal additive manufacturing in aircraft: Current application, opportunities and challenges. IOP Conf Ser Mater Sci Eng. https://doi.org/10.1088/1757-899X/493/1/012032
31. Zerbst U, Bruno G, Buffière JY, Wegener T, Niendorf T, Wu T, Zhang X, Kashaev N, Meneghetti G, Hrabe N, Madia M, Werner T, Hilgenberg K, Koukolíková M, Procházka R, Džugan J, Möller B, Beretta S, Evans A, Wagener R, Schnabel K (2021) Damage tolerant design of additively manufactured metallic components subjected to cyclic loading: State of the art and challenges. Prog Mater Sci. https://doi.org/10.1016/j.pmatsci.2021.100786
32. Gardner L (2023) Metal additive manufacturing in structural engineering – review, advances, opportunities and outlook. Structures 47:2178–2193. https://doi.org/10.1016/J.ISTRUC.2022.12.039
33. Gunasegaram DR, Steinbach I (2021) Modelling of microstructure formation in metal additive manufacturing: Recent progress, research gaps and perspectives. Metals (Basel). https://doi.org/10.3390/met11091425
34. Bajaj P, Hariharan A, Kini A, Kürnsteiner P, Raabe D, Jägle EA (2020) Steels in additive manufacturing: A review of their microstructure and properties. Mater Sci Eng. https://doi.org/10.1016/j.msea.2019.138633
35. Brennan MC, Keist JS, Palmer TA (2021) Defects in metal additive manufacturing processes. J Mater Eng Perform 30:4808–4818. https://doi.org/10.1007/s11665-021-05919-6
36. Sanaei N, Fatemi A (2021) Defects in additive manufactured metals and their effect on fatigue performance: A state-of-the-art review. Prog Mater Sci. https://doi.org/10.1016/j.pmatsci.2020.100724
37. Weeger O, Boddeti N, Yeung SK, Kaijima S, Dunn ML (2019) Digital design and nonlinear simulation for additive manufacturing of soft lattice structures. Addit Manuf 25:39–49. https://doi.org/10.1016/j.addma.2018.11.003
38. Wu W, Xia R, Qian G, Liu Z, Razavi N, Berto F, Gao H (2023) Mechanostructures: rational mechanical design, fabrication, performance evaluation, and industrial application of advanced structures. Prog Mater Sci. https://doi.org/10.1016/j.pmatsci.2022.101021
39. Jiang P, Rifat M, Basu S (2020) Impact of surface roughness and porosity on lattice structures fabricated by additive manufacturing- a computational study. Procedia Manuf 48:781–789. https://doi.org/10.1016/J.PROMFG.2020.05.114
40. Yánez A, Fiorucci MP, Cuadrado A, Martel O, Monopoli D (2020) Surface roughness effects on the fatigue behaviour of gyroid cellular structures obtained by additive manufacturing.

Int J Fatigue 138:105702. https://doi.org/10.1016/J.IJFATIGUE.2020.105702
41. Alomar Z, Concli F (2020) A review of the selective laser melting lattice structures and their numerical models. Adv Eng Mater 22:2000611. https://doi.org/10.1002/ADEM.202000611
42. de Pastre MA, Quinsat Y (2023) Virtual volume correlation of lattice structures: From volumetric data to geometrical and dimensional defects identification. Addit Manuf. https://doi.org/10.1016/j.addma.2022.103347
43. Rodríguez-Aparicio R, Alegre JM, Verbeeten WMH, Lorenzo-Bañuelos M, Cuesta II (2023) Methodology to predict mechanical properties of PA-12 lattice structures manufactured by powder bed fusion. Addit Manuf. https://doi.org/10.1016/j.addma.2023.103864
44. Murchio S, Dallago M, Zanini F, Carmignato S, Zappini G, Berto F, Maniglio D, Benedetti M (2021) Additively manufactured Ti–6Al–4V thin struts via laser powder bed fusion: Effect of building orientation on geometrical accuracy and mechanical properties. J Mech Behav Biomed Mater. https://doi.org/10.1016/j.jmbbm.2021.104495
45. Benedetti M, du Plessis A, Ritchie RO, Dallago M, Razavi N, Berto F (2021) Architected cellular materials: A review on their mechanical properties towards fatigue-tolerant design and fabrication. Mater Sci Eng R Rep. https://doi.org/10.1016/j.mser.2021.100606
46. Li M, Song Y, Yang X, Zhang K (2023) Lattice structure design optimization under localized linear buckling constraints. Comput Struct. https://doi.org/10.1016/j.compstruc.2023.107112
47. Viswanath A, Khalil M, Al Maskari F, Cantwell WJ, Khan KA (2023) Harnessing buckling response to design lattice structures with improved buckling strength. Mater Des. https://doi.org/10.1016/j.matdes.2023.112113
48. Zhao M, Li X, Zhang DZ, Zhai W (2023) Design, mechanical properties and optimization of lattice structures with hollow prismatic struts. Int J Mech Sci. https://doi.org/10.1016/j.ijmecsci.2022.107842
49. Veloso F, Gomes-Fonseca J, Morais P, Correia-Pinto J, Pinho ACM, Vilaça JL (2022) Overview of methods and software for the design of functionally graded lattice structures. Adv Eng Mater. https://doi.org/10.1002/adem.202200483
50. Jeong HS, Lyu SK, Park SH (2021) Effective strut-based design approach of multi-shaped lattices using equivalent material properties. J Mech Sci Technol 35:1609–1622. https://doi.org/10.1007/s12206-021-0324-7
51. Boursier Niutta C, Paolino DS, Tridello A (2023) Additively manufactured lattice structures: An innovative defect-based design methodology against crash impact. Eng Fail Anal. https://doi.org/10.1016/J.ENGFAILANAL.2023.107436
52. Kamranfard MR, Darijani H, Khademzadeh S (2024) Mechanical behavior of Ti6Al4V lattice structures; numerical and experimental analysis. Mech Adv Mater Struct 31:735–748. https://doi.org/10.1080/15376494.2022.2120651
53. Suard M, Martin G, Lhuissier P, Dendievel R, Vignat F, Blandin JJ, Villeneuve F (2015) Mechanical equivalent diameter of single struts for the stiffness prediction of lattice structures produced by Electron Beam Melting. Addit Manuf 8:124–131. https://doi.org/10.1016/j.addma.2015.10.002
54. Jiang P, De Meter EC, Basu S (2021) The influence of defects on the elastic response of lattice structures resulting from additive manufacturing. Comput Mater Sci 199:110716. https://doi.org/10.1016/J.COMMATSCI.2021.110716
55. Somnic J, Jo BW (2022) Status and challenges in homogenization methods for lattice materials. Materials. https://doi.org/10.3390/ma15020605
56. Glaesener RN, Kumar S, Lestringant C, Butruille T, Portela CM, Kochmann DM (2023) Predicting the influence of geometric imperfections on the mechanical response of 2D and 3D periodic trusses. Acta Mater. https://doi.org/10.1016/j.actamat.2023.118918
57. Tridello A, Boursier Niutta C, Benelli A, Paolino DS (2024) Absorbing capabilities of additively manufactured lattice structure specimens for crash applications: Damage tolerant design and simulations. Fatigue Fract Eng Mater Struct. https://doi.org/10.1111/FFE.14320
58. Della Ripa M, Paolino DS, Amorese A, Tridello A (2021) Numerical modelling of the mechanical response of lattice structures produced through AM. Procedia Structural Integrity. https://doi.org/10.1016/j.prostr.2021.10.079
59. Colombo C, Tridello A, Pagnoncelli AP, Biffi CA, Fiocchi J, Tuissi A, Vergani LM, Paolino DS (2023) Efficient experimental methods for rapid fatigue life estimation of additive manufactured elements. Int J Fatigue 167:107345. https://doi.org/10.1016/J.IJFATIGUE.2022.107345
60. Schreier H, Orteu JJ, Sutton MA (2009) Image correlation for shape, motion and deformation measurements: Basic concepts, theory and applications, Image Correlation for Shape, Motion and Deformation Measurements: Basic Concepts Theory and Applications. Springer, US, Boston, MA
61. Carraturo M, Alaimo G, Marconi S, Negrello E, Sgambitterra E, Maletta C, Reali A, Auricchio F (2021) Experimental and Numerical Evaluation of Mechanical Properties of 3D-Printed Stainless Steel 316L Lattice Structures. J Mater Eng Perform 30:5247–5251. https://doi.org/10.1007/S11665-021-05737-W/FIGURES/6
62. Magarò P, Alaimo G, Carraturo M, Sgambitterra E, Maletta C (2023) A novel methodology for the prediction of the stress–strain response of laser powder bed fusion lattice structure based on a multi-scale approach. Mater Sci Eng: A. https://doi.org/10.1016/j.msea.2022.144526
63. Oliver WC, Pharr GM (1992) An improved technique for determining hardness and elastic modulus using load and displacement sensing indentation experiments. J Mater Res. https://doi.org/10.1557/JMR.1992.1564
64. Ciampaglia A (2023) Data driven statistical method for the multiscale characterization and modelling of fiber reinforced composites. Compos Struct 320:117215. https://doi.org/10.1016/J.COMPSTRUCT.2023.117215
65. Smith M, Guan Z, Cantwell WJ (2013) Finite element modelling of the compressive response of lattice structures manufactured using the selective laser melting technique. Int J Mech Sci 67:28–41. https://doi.org/10.1016/J.IJMECSCI.2012.12.004